1 # Improving thermodynamic profile retrievals from microwave

2 # radiometers by including Radio Acoustic Sounding System (RASS)

3 # observations

4

5

6 Irina V. Djalalova[1,2], David D. Turner[3], Laura Bianco[1,2],

7 James M. Wilczak[2], James Duncan[1,2*], Bianca Adler[1,2] and Daniel Gottas[2]

8

9 [1] Cooperative Institute for Research in Environmental Sciences (CIRES), Boulder, CO, USA

10 [2] National Oceanic and Atmospheric Administration, Physical Sciences Laboratory, Boulder, CO, USA

11 [3] National Oceanic and Atmospheric Administration, Global Systems Laboratory, Boulder, CO USA

12 [*] Now at WindESCo, Burlington, MA

13

14

15

16

17

18 Corresponding author address: Irina V. Djalalova (Irina.V.Djalalova@noaa.gov), NOAA/Physical

19 Science Laboratory, 325 Broadway, mail stop: PSD3, Boulder, CO 80305. Tel.: 303-497-6238.

20 Fax: 303-497-6181.

21

44   **Abstract**

45   Thermodynamic profiles are often retrieved from the multi-wavelength brightness

46   temperature observations made by microwave radiometers (MWRs) using regression methods

47   (linear, quadratic approaches), artificial intelligence (neural networks), or physical-iterative

48   methods. Regression and neural network methods are tuned to mean conditions derived from

49   a climatological dataset of thermodynamic profiles collected nearby. In contrast, physical-

50   iterative retrievals use a radiative transfer model starting from a climatologically reasonable

51   profile of temperature and water vapor, with the model running iteratively until the derived

52   brightness temperatures match those observed by the MWR within a specified uncertainty.

53   In this study, a physical-iterative approach is used to retrieve temperature and humidity

54   profiles from data collected during XPIA (eXperimental Planetary boundary layer Instrument

55   Assessment), a field campaign held from March to May 2015 at NOAA's Boulder Atmospheric

56   Observatory (BAO) facility. During the campaign, several passive and active remote sensing

57   instruments as well as in-situ platforms were deployed and evaluated to determine their

58   suitability for the verification and validation of meteorological processes. Among the deployed

59   remote sensing instruments were a multi-channel MWR, as well as two radio acoustic sounding

60   systems (RASS), associated with 915-MHz and 449-MHz wind profiling radars.

61   In this study the physical-iterative approach is tested with different observational

62   inputs: first using data from surface sensors and the MWR in different configurations, and then

63   including data from the RASS into the retrieval with the MWR data. These temperature

64   retrievals are assessed against co-located radiosonde profiles. Results show that the

65   combination of the MWR and RASS observations in the retrieval allows for a more accurate

3

66   characterization of low-level temperature inversions, and that these retrieved temperature

67   profiles match the radiosonde observations better than the temperature profiles retrieved from

68   only the MWR in the layer between the surface and 3 km above ground level (AGL). Specifically,

69   in this layer of the atmosphere, both root mean square errors and standard deviations of the

70   difference between radiosonde and retrievals that combine MWR and RASS are improved by

71   mostly 10-20% compared to the configuration that does not include RASS observations.

72   Pearson correlation coefficients are also improved.

73   A comparison of the temperature physical retrievals to the manufacturer-provided neural

74   network retrievals is provided in Appendix A.

75

76

77

78

79

80

81

82

83

84

85

86

87

1. Introduction

88

89   Monitoring the state of the atmosphere for process understanding and for model

90 verification and validation requires observations from a variety of instruments, each one having

91 its set of advantages and disadvantages. Using several diverse instruments allows one to

92 monitor different aspects of the atmosphere, while combining them in an optimized synergetic

93 approach can improve the accuracy of the information available on the state of the

94 atmosphere.

95   During the eXperimental Planetary boundary layer Instrumentation Assessment (XPIA)

96 campaign, a U.S. Department of Energy sponsored experiment held at the Boulder Atmospheric

97 Observatory (BAO) in Spring 2015, several instruments were deployed (Lundquist et al., 2017)

98 with the goal of assessing their capability for measuring atmospheric boundary layer

99 meteorological variables. XPIA investigated novel measurement approaches, and quantified

100 uncertainties associated with these measurement methods. While the main interest of the XPIA

101 campaign was on wind and turbulence, measurements of other important atmospheric

102 variables were also collected, including temperature and humidity. Among the deployed

103 instruments were two identical microwave radiometers (MWRs) and two radio acoustic

104 sounding systems (RASS), as well as radiosondes launches.

105   MWRs are passive sensors, sensitive to atmospheric temperature and humidity content

106 that allow for a high temporal observation of the state of the atmosphere, with some

107 advantages and limitations. In order to estimate profiles of temperature and humidity from the

108 observed brightness temperatures (Tb), several methods could be applied such as regressions,

109 neural network retrievals, or physical retrieval methodologies which can include additional

110   information about the atmospheric state in the retrieval process (e.g., Maahn et al. 2020).

111   Microwave radiative transfer models (e.g., Rosenkranz, 1998; Clough et al. 2005) are commonly

112   used to train statistical retrievals, or as forward models used within physical retrieval methods.

113   Advantages of MWRs include their compact design, the relatively high temporal resolution of

114   the measurements (2-3 minutes), the possibility to observe the vertical structure of both

115   temperature and moisture through the lower part of the troposphere during both clear and

116   cloudy conditions, and their capability to operate in a standalone mode. Disadvantages include

117   limited accuracy in the presence of rain because of scattering of radiation from raindrops in the

118   atmosphere (and because water can deposit on the radome, although the instruments use a

119   hydrophobic radome and force airflow over the surface of the radome during rain to mitigate

120   this impact), rather coarse vertical resolution, and for retrievals the necessity to have a site-

121   specific climatology. Other disadvantages include the challenges related to performing accurate

122   calibrations (Küchler et al., 2016, and references within), radio frequency interference (RFI), and

123   the low accuracy on the retrieved liquid water path (LWP) especially for values of LWP less than

124   20 g m^{-2} (Turner 2007; Turner et al. 2007).

125   RASS, in comparison, are active instruments that emit a longitudinal acoustic wave

126   upward, causing a local compression and rarefaction of the ambient air. These density

127   variations are tracked by the Doppler radar associated with the RASS, and the speed of the

128   propagating sound wave is measured. The speed of sound is related to the virtual temperature

129   (Tv) (North et al., 1973), and therefore, RASS are used to remotely measure vertical profiles of

130   virtual temperature in the boundary layer. Being an active instrument, the RASS is in general

131   more accurate than a passive instrument (Bianco et al., 2017), but they also come with their

132   own disadvantages. The main limitations of RASS for temperature measurements are the low

133   temporal resolution (typically a 5-min averaged RASS profile is measured once or twice per

134   hour), their limited altitude coverage, and the noise "pollution" that impacts local communities.

135   Adachi and Hashiguchi (2019) have shown that RASS could use parametric speakers to take

136   advantage of their high directivity and very low side lobes. Nevertheless, the maximum height

137   reached by the RASS is still limited, being a function of both radar frequency and atmospheric

138   conditions (May and Wilczak, 1993). It is determined both by the attenuation of the sound,

139   which is a function of atmospheric temperature, humidity, and frequency of the sound source,

140   and the advection of the propagating sound wave out of the radar's field-of-view. Therefore,

141   data availability is usually limited to the lowest several kilometers, depending on the frequency

142   of the radar. In addition, wintertime coverage is usually lower than that in summer, due to

143   increased attenuation of the acoustic signal in cooler and drier environments.

144   To get a better picture of the state of the temperature and moisture structure of the

145   atmosphere, it makes sense to try to combine the information obtained by both MWR and

146   RASS. Integration of different instruments has been a topic of ongoing scientific interest (Han

147   and Westwater 1995; Stankov et al. 1996; Bianco et al., 2005; Engelbart et al., 2009; Cimini et

148   al., 2020; Turner and Löhnert, 2021, to name some). In this study, the focus is on the

149   combination of the MWR and RASS observations in the retrievals to improve the accuracy of

150   the temperature profiles in the lowest 3 km compared to physical retrieval approaches that do

151   not include the information from RASS measurements. Some studies have used analyses from

152   numerical weather prediction (NWP) models as an additional constraint in these variational

153   retrievals (e.g., Hewison 2007; Cimini et al. 2005, 2011; Martinet et al. 2020); however, we have

154   elected not to include model data in this study because we wanted to evaluate the impact of

155   the RASS profiles on the retrievals from a purely observational perspective.

156   This paper is organized as follows: Section 2 summarizes the experimental dataset;

157   Section 3 introduces the principles of the physical retrieval approaches used to obtain vertical

158   profiles of the desired variables; Section 4 produces statistical analysis of the comparison

159   between the different retrieval approaches and radiosonde measurement; finally, conclusions

160   are presented in Section 5.

161

162   **2. XPIA dataset**

163   The data used in our analysis were collected during the XPIA experiment, held in Spring

164   2015 (March-May) at NOAA's BAO site, in Erie, Colorado (Lat.: 40.0451 N, Lon.: 105.0057 W, El.:

165   1584 m MSL). XPIA was the last experiment conducted at this facility, as after almost 40 years

166   of operations the BAO 300-m tower was demolished at the end of 2016 (Wolfe and Lataitis,

167   2018). XPIA was designed to assess the capability of different remote sensing instruments for

168   quantifying boundary layer structure, and was a preliminary study as many of these same

169   instruments were later deployed, among other campaigns, for the second Wind Forecast

170   Improvement Project WFIP2 (Shaw et al., 2019; Wilczak et al., 2019) which investigated flows in

171   complex terrain for wind energy applications, where they were for example used to study cold

172   air pools (Adler et al., 2021) and gap flow characteristics (Neiman et al., 2019; Banta et al.,

173   2020). The list of the deployed instruments included active and passive remote-sensing devices,

174   and in-situ instruments mounted on the BAO tower. Data collected during XPIA are publicly

175   available at https://a2e.energy.gov/projects/xpia. A detailed description of the XPIA

176   experiment can be found in Lundquist et al. (2017), while a specific look at the accuracy of the

177   instruments used in this study can be found in Bianco et al. (2017).

178

179   **2.1 MWR measurements**

180   Two identical MWRs (Radiometrics MP-3000A) managed by NOAA (MWR-NOAA) and by

181   the University of Colorado (MWR-CU), were deployed next to each other at the visitor center

182   ~600 m south of the BAO tower (see Lundquist et al., 2017 for a detailed map of the study

183   area). Prior to the experiment, both MWRs were thoroughly serviced (sensor cleaning, radome

184   replacement, etc.) and calibrated using an external liquid nitrogen target and an internal

185   ambient target. MWRs are passive devices which record the natural microwave emission in the

186   water vapor and oxygen absorption bands from the atmosphere, providing measurements of

187   the brightness temperatures. Both MWRs have 35-channels spanning a range of frequencies,

188   with 21 channels in the lower (22-30 GHz) K-band frequency band, of which 8 channels were

189   used during XPIA: 22.234, 22.5, 23.034, 23.834, 25, 26.234, 28 and 30 GHz; and 14 channels in

190   the higher (51-59 GHz) V-band frequency band, of which all were used in XPIA: 51.248, 51.76,

191   52.28, 52.804, 53.336, 53.848, 54.4, 54.94, 55.5, 56.02, 56.66, 57.288, 57.964 and 58.8 GHz.

192   Frequencies in the K-band are more sensitive to water vapor and cloud liquid water, while

193   frequencies in the V-band are sensitive to atmospheric temperature due to the absorption of

194   atmospheric oxygen (Cadeddu et al., 2013). V-band frequencies or channels can also be divided

195   in two categories: the opaque channels, 56.66 GHz and higher, that are more informative in the

196   layer of the atmosphere from the surface to ~1 km AGL, and the transparent channels, 51-56

197   GHz, that are more informative above 1 km AGL. Both MWRs observed at the zenith and at 15-

198   and 165-degree elevation angles in the north-south plane (referred to as oblique elevation

199   scans and used as their average hereafter; note zenith views have a 90-degree elevation angle).

200   However, when MWRs are deployed in locations with unobstructed views, oblique scans can be

201   performed down to 5 degrees elevation angles and may provide better temperature profile

202   accuracy in the lowest 0-1 or even 0-2 km AGL layers (Crewell and Löhnert, 2007).

203   In addition, each MWR was provided with a separate surface sensor to measure

204   pressure, temperature, and relative humidity at the installation level that was ~2.5 m AGL.

205   Vertical profiles of temperature (T), water vapor density (WVD), and relative humidity (RH)

206   were retrieved in real-time during XPIA every 2-3 minutes using a neural network (NN)

207   approach provided by the manufacturer of the radiometer (Solheim et al. 1998a, and 1998b;

208   Ware et al., 2003). Although the physical retrieval configurations used in this study do not

209   exactly match the NN retrieval configurations, a comparison of both physical and neural

210   network retrievals to the radiosonde temperature data is presented in Appendix A.

211   Both MWRs nominally operated from 9 March to 7 May 2015, although the MWR-NOAA

212   was unavailable between 5-27 April 2015. For the overlapping dates, temperature profiles

213   retrieved from the two MWRs showed very good agreement with less than 0.5 ^{o}C bias and

214   0.994 correlation (Bianco et al., 2017). For this reason, and because the MWR-CU was available

215   for a longer time period, only the MWR-CU (hereafter simply called MWR) is used.

216

217   **2.2 WPR-RASS measurements**

218   Two NOAA wind profiling radars (WPRs), operating at frequencies of 915-MHz and 449-

219   MHz, were deployed at the visitor center (same location as the MWR) during XPIA. These

220 systems are primarily designed to measure the vertical profile of the horizontal wind vector, but

221 co-located RASS also enable the observation of profiles of virtual temperature in the lower

222 atmosphere, with different resolutions and height coverages depending on the WPR. Thus, the

223 RASS associated with the 915-MHz WPR (hereafter referred to as RASS 915) measured virtual

224 temperature from 120 to 1618 m with a vertical resolution of 62 m, and the 449 MHz RASS

225 (hereafter referred to as RASS 449) sampled the boundary layer from 217 to 2001 m with a

226 vertical resolution of 105 m. The maximum height reached by the RASS is a function of both

227 radar frequency and atmospheric conditions (May and Wilczak, 1993), and is usually lower for

228 RASS 915 data, as will be shown later in the analysis.

229   The RASS data were processed using a radio frequency interference (RFI)-removal

230 algorithm (performed on the RASS spectra), a consensus algorithm (Strauch et al. 1984)

231 performed on the moment data using a 60% consensus threshold, a Weber-Wuertz outlier

232 removal algorithm (Weber et al., 1993) performed on the consensus averages, and a RASS

233 range-correction algorithm (Görsdorf and Lehmann, 2000) using an average relative humidity

234 setting of 50% determined from the available observations.

235

236 **2.3 BAO data**

237   The BAO 300-m tower was built in 1977 to study the planetary boundary layer (Kaimal

238 and Gaynor 1983). During XPIA, measurements were collected at the surface (2 m) and at six

239 higher levels (50, 100, 150, 200, 250 and 300 m AGL). Each tower level was equipped with 2

240 sonic anemometers on orthogonal booms, and one sensor based on a Sensiron SHT75 solid-

241 state sensor to measure temperature and relative humidity with a time resolution of 1 s, and

242   averaged over five minutes. The more accurate temperature and water vapor observations

243   (Horst et al., 2016) at the BAO tower 2 m AGL level are used in the physical retrieval in place of

244   the less accurate MWR inline surface sensor.

245

246   **2.4 Radiosonde measurements**

247   Between 9 March and 7 May 2015, while the MWR was operational, radiosondes were

248   launched by the National Center for Atmospheric Research (NCAR) assisted by several students

249   from the University of Colorado over three selected periods, one each in March, April, and May.

250   All radiosondes were Vaisala model RS92. There was a total of 59 launches, mostly four times

251   per day, around 1400, 1800, 2200, and 0200 UTC (0800, 1200, 1600 and 2000 local standard

252   time, LST). The first 35 launches, between 9-19 March, were done from the visitor center, while

253   11 launches between 15-22 April, and 13 launches between 1-4 May, were done from the

254   water tank site, ~1000 meters away from the visitor center (see Lundquist et al., 2017 for a

255   detailed map of the study area). The radiosonde measurements included temperature, dew

256   point temperature, and relative humidity to altitudes usually higher than 10 km AGL, with

257   measurements every few seconds. As a first step, for additional verification, the radiosonde

258   data from the 59 launches taken between 9 March and 4 May 2015 were compared to the BAO

259   tower measurements, up to 300 m AGL. These observed data sets match very well, with a

260   correlation coefficient of 0.99 and a standard deviation of ~0.7 °C. However, one radiosonde

261   profile showed a large bias (> 5 °C) against all seven levels of BAO temperature measurements

262   and all available Tv measurements from the RASS 915 (eight measurements up to 600 m AGL)

263   and from the RASS 449 (nine measurements up to 1100 m AGL), therefore this particular

264 radiosonde profile was excluded from the statistical analysis. Moreover, while accurate RASS

265 data can be collected during rain, MWR data could be potentially deteriorated due to water

266 deposition on the radome. Therefore, six profiles (three for March 13, and one each on May 1,

267 3 and 4) were eliminated from the statistical evaluation. These restrictions lowered the number

268 of total radiosonde launches used in this study to 52.

269

270 **3. Physical retrievals**

271   One way to combine the active and passive instruments would be to use the RASS

272 observations up to their maximum available height, and stitch them with the profiles obtained

273 from a physical-iterative method using MWR data. To do this, the moisture contribution to the

274 RASS virtual temperatures could be removed by using either the relative humidity measured by

275 the MWR or by a climatology of the moisture term. However, merging these different profiles

276 could result in artificial jumps at the connecting heights.

277   Alternatively, a physical retrieval (PR) iterative approach can be used to retrieve vertical

278 profiles of thermodynamic properties from the MWR and RASS observations in a synergistic

279 manner (e.g., Maahn et al 2020; Turner and Löhnert 2021). In this case, an optimal estimation-

280 based physical retrieval is initialized with a climatologically reasonable profile of temperature

281 and water vapor, and is iteratively repeated until the computed brightness temperatures match

282 those observed by the MWR within the uncertainty of the observed brightness temperatures

283 and the RASS virtual temperatures within their uncertainties (Rodgers, 2000; Turner and

284 Löhnert, 2014; Maahn et al. 2020).

285

3.1 Iterative retrieval technique

286

287   For this study, the PR uses the *TROPoe* retrieval algorithm (formerly *AERIoe*, Turner and

288 Löhnert 2014; Turner and Blumberg 2019; Turner and Löhnert 2021). This algorithm is able to

289 use radiance data from microwave radiometers, infrared spectrometers, and other

290 observations as input. The microwave radiative transfer model, MonoRTM (Clough et al., 2005),

291 serves as the forward model, which is fully functional for the microwave region and was

292 intensively evaluated previously on MWR measurements (Payne et al. 2008; 2011).

293   We start with the state vector $\mathbf{X_a}$ = [$\mathbf{T, Q,}$ LWP]^T, where superscript T denotes transpose,

294 and vectors and matrices are shown in bold. $\mathbf{T}$ (K) and $\mathbf{Q}$ (g kg^{-1}) are temperature and water

295 vapor mixing ratio profiles at 55 vertical levels from the surface up to 17 km, with the distance

296 between the levels increasing geometrically with height. LWP is the liquid water path in (g m^{-2})

297 that measures the integrated content of liquid water in the entire vertical column above the

298 MWR, and is a scalar. For this study, $\mathbf{X_a}$ has dimensions equal to 111 x 1 (two vectors $\mathbf{T}$ and $\mathbf{Q}$

299 with 55 levels each, and LWP). The retrieval framework of Turner and Blumberg (2019) is used,

300 but only using MWR data (no spectral infrared). Here, we demonstrate the augmentation of the

301 retrieval to include RASS profiles of $\mathbf{Tv}$, and the resulting impact this has on the retrieved

302 temperature profiles and information content.

303   The observation vector $\mathbf{Y}$ includes temperature and water vapor mixing ratio measured

304 at the surface in-situ, and spectral $\mathbf{Tb}$ measured by the MWR. The MonoRTM model $\mathbf{F}$ is used as

305 the forward model from the current state vector $\mathbf{X}$, and is then compared to the observation

306 vector $\mathbf{Y,}$ iterating until the difference between $\mathbf{F(X)}$ and $\mathbf{Y}$ is small within a specified uncertainty

307 (Eq 1).

308

$$X_{n+1} = X_n + (S_a^{-1} + K^T S_\varepsilon^{-1} K)^{-1} K^T S_\varepsilon^{-1} [Y - F(X_n) + K(X_n - X_a)] \quad (1)$$

310   with

$$X_a = \begin{bmatrix} T \\ Q \\ LWP \end{bmatrix} \qquad S_a = \begin{bmatrix} \sigma_{TT}^2 & \sigma_{TQ}^2 & 0 \\ \sigma_{QT}^2 & \sigma_{QQ}^2 & 0 \\ 0 & 0 & \sigma_{LWP}^2 \end{bmatrix} \qquad K_{ij} = \partial F_i \Big/ \partial X_j$$

311

312   where i and j in the $\mathbf{K}_{ij}$ definition mark channel and vertical level, respectively. The superscripts

313   T and -1 in (1) indicate the transpose and inverse matrix, respectively. The observation vector **Y**

314   and the covariance matrix of the observed data, $\mathbf{S_\varepsilon}$, depending on the configuration used, are

315   equal to:

$$Y_1 = \begin{bmatrix} T_{sfc} \\ Q_{sfc} \\ Tb_{zenith} \end{bmatrix} \qquad S_{\varepsilon_1} = \begin{bmatrix} \sigma_{Tsfc}^2 & 0 & 0 \\ 0 & \sigma_{Qsfc}^2 & 0 \\ 0 & 0 & \sigma_{Tb_{zenith}}^2 \end{bmatrix}$$

316

$$Y_2 = \begin{bmatrix} T_{sfc} \\ Q_{sfc} \\ Tb_{zenith+oblique} \end{bmatrix} \qquad S_{\varepsilon_2} = \begin{bmatrix} \sigma_{Tsfc}^2 & 0 & 0 \\ 0 & \sigma_{Qsfc}^2 & 0 \\ 0 & 0 & \sigma_{Tb_{zenith+oblique}}^2 \end{bmatrix}$$

317

$$Y_3 = \begin{bmatrix} T_{sfc} \\ Q_{sfc} \\ Tb_{zenith+oblique} \\ Tv_{RASS915} \end{bmatrix} \qquad S_{\varepsilon_3} = \begin{bmatrix} \sigma_{Tsfc}^2 & 0 & 0 & 0 \\ 0 & \sigma_{Qsfc}^2 & 0 & 0 \\ 0 & 0 & \sigma_{Tb_{zenith+oblique}}^2 & 0 \\ 0 & 0 & 0 & \sigma_{Tv_{RASS915}}^2 \end{bmatrix}$$

318

319 $$Y_4 = \begin{bmatrix} T_{sfc} \\ Q_{sfc} \\ Tb_{zenith+oblique} \\ Tv_{RASS449} \end{bmatrix} \quad S_{\varepsilon_4} = \begin{bmatrix} \sigma^2_{Tsfc} & 0 & 0 & 0 \\ 0 & \sigma^2_{Qsfc} & 0 & 0 \\ 0 & 0 & \sigma^2_{Tb_{zenith+oblique}} & 0 \\ 0 & 0 & 0 & \sigma^2_{Tv_{RASS449}} \end{bmatrix}$$

320   Note that the 2-m surface-level observations of temperature and water vapor mixing

321   ratio (T_{sfc} and Q_{sfc}, respectively) are included as part of the observation vector **Y**, and thus the

322   uncertainties (0.5 K for temperature and less than 0.4 g kg^{-1} for mixing ratio) in these

323   observations are included in S_ε.

324   The mean state vector of the climatological estimates, or a "prior" vector X_a, is a key

325   component in the optimal estimation framework and it is the first guess of the state vector **X**,

326   X_1 in Eq. (1). It provides a constraint on the ill-posed inversion problem. The prior is calculated

327   independently for each month of the year from climatological sounding profiles (using 10 years

328   of data) in the Denver area. The covariance matrix, S_a, of the "prior" vector includes not only

329   temperature or water vapor variances but also the covariances between them. Using around

330   3,000 radiosondes launched by the NWS in Denver, each radiosonde profile is interpolated to

331   the vertical levels used in the retrieval, after which the covariance of temperature and

332   temperature, temperature and humidity, and humidity and humidity is computed for different

333   levels.

334   Four configurations are chosen for the observational vector **Y** (Y_1, Y_2, Y_3, and Y_4). In each

335   of these, the surface observations are obtained by the 2-m BAO *in-situ* measurements of

336   temperature and humidity. The MWR provides **Tb** measurements from 22 channels from the

337   zenith scan for the zenith only configuration (Y_1), while when using the zenith plus oblique Tb

16

338   inputs (Y_2, Y_3, and Y_4) the same 22 channels were used from the zenith scans together with only

339   the four opaque channels (56.66, 57.288, 57.964 and 58.8 GHz) from the oblique scans. Using

340   additional measurements from the co-located radar systems with RASS, the observational

341   vector is further expanded with either RASS 915 (Y_3) or RASS 449 (Y_4) virtual temperature

342   observations. The covariance matrix of the observed data, S_ε, depends on the chosen Y_i as seen

343   in the matrix $S_{\varepsilon i}$ (with i = 1:4) descriptions, with increasing dimensions from Y_1 to Y_2 and

344   additional increasing dimensions to Y_3 or Y_4 through the multi-level measurements of the RASS

345   (Turner and Blumberg, 2019). Table 1 summarizes the observational information included in

346   these four different configurations of the PR.

347

	T_{sfc}	Q_{sfc}	Tb_{zenith}	$Tb_{oblique}$	$Tv_{RASS915}$	$Tv_{RASS449}$
Y_1 = MWRz	X	X	X			
Y_2 = MWRzo	X	X	X	X		
Y_3 = MWRzo915	X	X	X	X	X	
Y_4 = MWRzo449	X	X	X	X		X

348   *Table 1. Four PR configurations corresponding to the four observational Y_i vectors in Eq. (1).*

349

350   The uncertainty in the MWR Tb observations was set to the standard deviation from a

351   detrended time-series analysis for each channel during cloud-free periods. The method to

17

352   detect those cloud-free periods is described in detail in Section 3.2. The derived uncertainties

353   ranged from 0.3 K to 0.4 K in the 22 to 30 GHz channels, and 0.4 to 0.8 K in the 52 to 60 GHz

354   channels. We assumed that there was no correlated error between the different MWR

355   channels.

356   For the RASS, co-located RASS and radiosonde profiles were compared and the standard

357   deviation of the differences in Tv were determined as a function of the radar's signal-to-noise

358   ratio (SNR). This relationship resulted in uncertainties that ranged from 0.8 K at high SNR values

359   to 1.5 K at low SNR values. Again, we assumed that there was no correlated error between

360   different RASS heights. Following these assumptions, the covariance matrix $\mathbf{S_\varepsilon}$ is diagonal.

361   The Jacobian matrix, $\mathbf{K}$, is computed using finite differences by perturbing the elements

362   of $\mathbf{X}$ and rerunning the forward model. It has dimensions m x 111, where m is the length of the

363   vector $\mathbf{Y_i}$, therefore its dimension increases correspondingly with the inclusion of more

364   observational data. $\mathbf{K}$ makes the "connection" between the state vector and the observational

365   data and should be calculated at every iteration.

366

367   **3.2 Bias-correction of MWR observations using radiosondes or climatology**

368   Observational errors propagate through retrieval into the derived profiles (i.e. the bias

369   of the observed data will contribute to a bias in the retrievals). For that, retrieval uncertainties

370   in Eq. (1) from $\mathbf{Y} = \mathbf{Y_1}$ or $\mathbf{Y_2}$ derive only from uncertainties in surface and MWR data, while

371   retrieval uncertainties from $\mathbf{Y} = \mathbf{Y_3}$ or $\mathbf{Y_4}$ come from uncertainties in the surface, MWR, and RASS

372   measurements.

373   The bias of the retrieval depends on both the absolute accuracy of the forward model

374   and on any observational systematic offset, of which the systematic error in the MWR

375   observations could potentially be reduced through application of a MWR Tb bias-correction

376   procedure. In this study, two different approaches were used for the bias-correction: the first is

377   based on a comparison to the radiosondes, while the second uses climatological profiles. The

378   first method could be used for a field campaign where occasional co-located radiosonde

379   launches are taken, while the second would be used for deployments without any supporting

380   radiosonde observations.

381   For both approaches, the first step is to identify clear-sky periods during which the bias

382   can be estimated (to reduce the degrees of freedom associated with clouds) and subsequently

383   the bias can be removed from the observed MWR Tbs. One method to identify clear-sky times

384   is to use a time-series of Tb observations in the 30 GHz liquid water sensitive channel of the

385   MWR.

386   The standard deviation of the MWR Tb in the 30 GHz channel is calculated over a time

387   frame of one hour centered at the radiosonde launch time. The data from the zenith scan and

388   the averaged oblique scans are reviewed separately. Liquid-cloud free periods were identified

389   by cases where the temporal standard deviation was small (< 0.4 K), and more than 35

390   radiosonde profiles were classified as being launched in clear skies. The usage of the standard

391   deviation from the time-series from the oblique scans, with the same 0.4 K restriction, reduces

392   the number of the clear-sky radiosonde profiles to 18. For those chosen 18 radiosonde profiles,

393   the Tb is calculated from radiosonde temperature profiles through MonoRTM at each of the

394   MWR channels. The mean difference between these calculated radiosonde Tbs and measured

395　MWR Tbs forms the Tb bias with which the MWR Tb data can be corrected. This bias-correction

396　method will be referred to as 'radiosonde BC'.

397　　　While this radiosonde BC method can be employed for the XPIA dataset, for other

398　campaigns this approach would not be possible if co-located radiosonde observations were not

399　available. For this situation, an alternative method for correcting the MWR Tb biases is

400　presented. In this method, to choose clear-sky periods, the 30 GHz channel MWR Tb data are

401　used on a daily basis. The standard deviation of the MWR Tb is calculated as the average of

402　standard deviations in a one-hour sliding window through all data points of a day. Four clear-

403　sky days were identified using a threshold of 0.4 K on the standard deviation: March 10 and 30,

404　and April 13 and 29, 2015. The Tb bias is then computed for each of the 22 channels as the

405　averaged difference between the observed Tb from the MWR zenith observations and the

406　forward model calculated Tbs at zenith using the TROPoe-retrieved profiles (Y_1) of those

407　selected clear-sky days. This method identified spectral calibration errors in the MWR

408　observations that could not be explained by physically realistic atmospheric profiles. This bias-

409　correction technique will be referred to as 'TROPoe BC'.

410　　　Fig. 1 shows the Tb biases found for all 22 MWR channels from both bias-correction

411　approaches. The biases calculated with the radiosonde BC scheme are shown for all channels

412　used in our analysis: 22 channels of the zenith scan, in red, and four V-band opaque channels of

413　the oblique scans, in blue. The black and green triangles represent the biases calculated using

414　the TROPoe BC approach for zenith and for zenith+oblique scans, respectively. All biases are

415　presented with associated uncertainties (error bars representing the standard deviation over all

20

416   radiosondes for radiosonde BC, and mean observation Tb vector uncertainties for chosen four

417   clear-sky days for TROPoe BC).

BIAS, Tb_OBS - Tb_CALCULATED
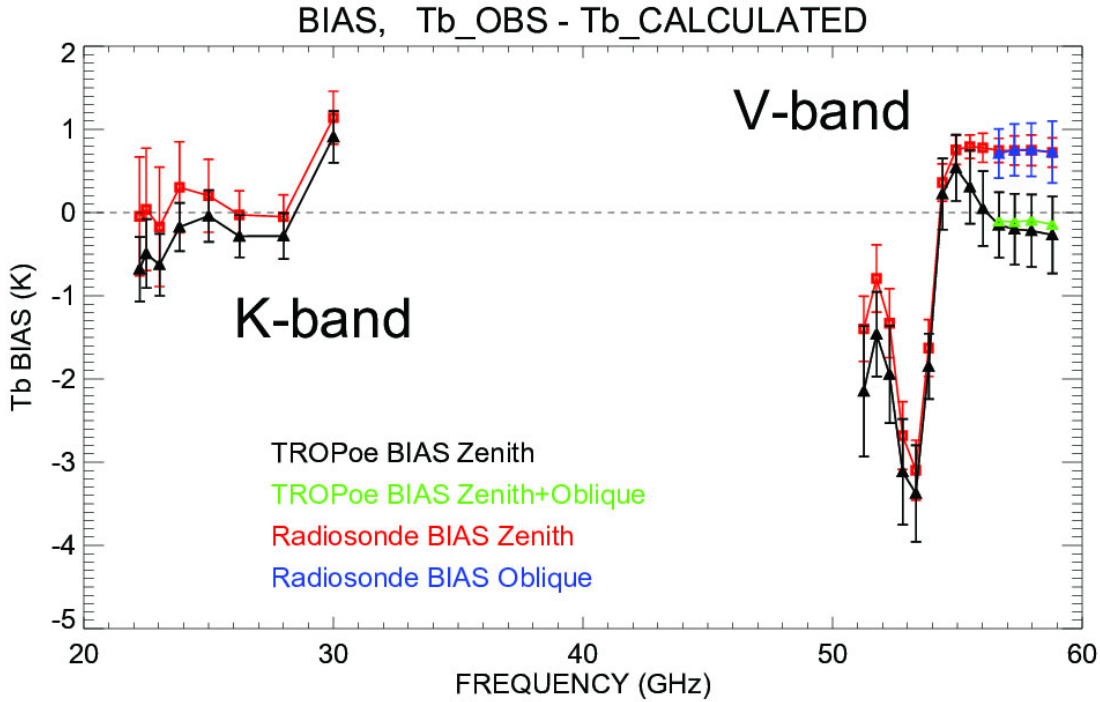
418   *Fig. 1. Tb biases derived from the radiosonde BC method (and TROPoe BC method) in all*

419   *22 MWR channels of the zenith scan in red (and in black), and in the four opaque channels of*

420   *the oblique scans in blue (and in green).*

421

422   The biases from the two bias-correction schemes are within the uncertainties of each

423   other for most of the channels except at the higher frequencies in the V-band. Biases in the

424   most opaque channels are significantly affected by the accuracy of the boundary layer

425   temperature profiles. When TROPoe BC is used, a monthly average prior temperature profile is

426   used in the PR, and thus differences between this prior profile and the actual temperature

427   profile can result in a spectral bias in the more opaque MWR channels. On the contrary, the

428   radiosonde BC uses a direct measurement of the temperature profile (from the radiosonde),

429   and thus is more accurate. It is also important to note that, in both approaches, the biases in

430   the opaque channels for zenith and for oblique scans (for radiosonde BC these are red and blue,

431   respectively; and for the TROPoe BC these are black and green, respectively) are very similar to

432   each other. This supports the assumption that the true bias is nearly independent of the scene,

433   or that the sensitivity to the scene (e.g., zenith or off-zenith) is small.

434   The bias-correction methods were applied by removing the corresponding calculated

435   biases from the MWR Tb observations before the retrievals were performed. Later in Section 4,

436   differences in the retrieved temperature profiles will be shown when using the two bias-

437   correction approaches. These differences will be more evident in the temperature profiles

438   exhibiting near-ground temperature inversions.

439   However, the final goal of this study is not to assess the sensitivity to different bias-

440   correction approaches but to verify that the inclusion of RASS observations does improve

441   retrieved temperature profiles, independently of the bias-correction method used.

442

443   **3.3 Analysis of physical retrieval characteristics**

444   The retrieved profiles of the four different PR configurations presented in Table 1

445   (MWRz, MWRzo, MWRzo915, MWRzo449) were compared to the radiosonde profiles. To

446   compare radiosonde observations against the PR profiles, all radiosonde profiles were

447   interpolated vertically to the same PR heights, and PR profiles were averaged in the time

448   window between 15 minutes before and 15 minutes after each radiosonde launch. Since the

449   radiosonde ascends quite quickly in the lowest kilometers of the atmosphere (~15-20 min to

450   reach 5 km), the 30-minute temporal window is estimated to be representative of the same

451   volume of the atmosphere measured by the radiosonde. BAO tower temperature and mixing

452   ratio data at the seven available levels were used as an additional validation dataset, without

453   any vertical interpolation, averaged in the time window between 15 minutes before and 15

454   minutes after each radiosonde launch.

455   As an example of the different temperature retrievals and their relative performance,

456   data obtained on 17 March 2015 at 2200 UTC are presented in Fig. 2. Temperature profiles up

457   to 2 km AGL retrieved from the four PR configurations (MWRz, MWRzo, MWRzo915,

458   MWRzo449, using the radiosonde BC) are compared to the radiosonde data in red and to the

459   BAO measurements in blue squares. Note that all four of the PRs match the BAO observations

460   reasonably well near the ground. The MWRz and MWRzo profiles are very smooth and depart

461   quite substantially from the radiosonde measurements, being unable to reproduce the more

462   detailed structure of the atmospheric temperature profile measured by the radiosonde, while

463   the MWRzo449 profile (in light-blue) demonstrates a better agreement with both the

464   radiosonde and BAO measurements (blue squares). The MWRzo915 profile (in purple) also tries

465   to follow the elevated temperature inversion observed by the radiosonde, successfully only in

466   the lower part of the atmosphere (below 1 km AGL) where RASS 915 measurements are

467   available. This behavior will be also addressed in the following section and in the statistical

468   analysis presented later in the manuscript.

469

20150317_220000
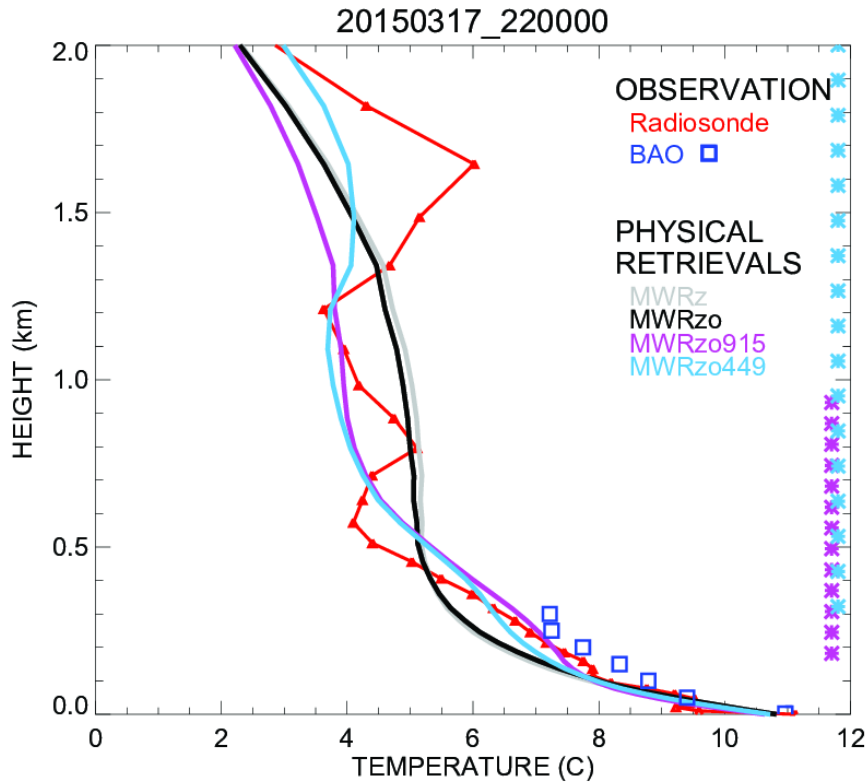
470

471 Fig. 2. Temperature profiles obtained by the four PR configurations, after applying the

472 radiosonde BC on the MWR Tbs: MWRz in gray, MWRzo in black, MWRzo915 in purple, and

473 MWRzo449 in light-blue. These retrievals are compared to radiosonde measurements, in red,

474 and BAO tower observations, in blue squares. The heights with available RASS virtual

475 temperature measurements (RASS 915 in purple and RASS 449 in light-blue) are marked by the

476 asterisks on the right Y-axis.

477

478 An asset of TROPoe is that several characteristics of the PRs can be obtained from two

479 matrices, the averaging kernel, **Akernel,** and the posterior covariance matrix, **Sop** (Masiello et

480 al., 2012; Turner and Löhnert, 2014, Turner and Bloomberg, 2019), calculated as:

481

24

482        $Akernel = B^{-1} K^T S_\varepsilon^{-1} K$ (2)

483   and:

484        $Sop = B^{-1}$ (3)

485   where:

486        $B = S_a^{-1} + K^T S_\varepsilon^{-1} K$

487

488   All matrices, **Akernel**, **Sop**, and **B**, have dimensions 111 x 111 in our configuration. While

489   the top left corner of the **Akernel** matrix (1:55, 1:55) is devoted to temperature, called further

490   in the text **ATkernel**, the next (56:110, 56:110) elements are devoted to the water vapor mixing

491   ratio, called **AQkernel**.

492   The **Akernel** provides useful information about the calculated retrievals, such as vertical

493   resolution and degrees of freedom for signal at each level. The rows of the **Akernel** provide the

494   smoothing functions (Rodgers, 2000) that could be applied to the radiosonde profiles (Eq. 4) to

495   minimize the vertical representativeness error in the comparison between the various retrievals

496   and the radiosonde profiles due to very different vertical resolutions of these profiles (Turner

497   and Löhnert, 2014).

498   Smoothed radiosonde observed profiles can be computed using the averaging kernel,

499   as:

500        $X_{smoothed\_radiosonde} = Akernel\ (X_{radiosonde} - X_a) + X_a$ (4)

501   The **Akernel** in Eq. (2) depends on the retrieval parameters (e.g., which datasets are

502   used in the **Y** vector, the values assumed in the observation covariance matrix S_ε, and the

503   sensitivity of the forward model), so for our four PR configurations it is possible to calculate

504   four different kernels from Eq. (2).

505   For each of the four **Akernel**s, a smoothed radiosonde profile can be computed for each

506   radiosonde profile using Eq. (4). In the presence of temperature inversions or other particular

507   structures in the atmosphere, these smoothed profiles can be quite different from each other

508   and also from the original unsmoothed radiosonde profile. Consequently, while comparison of

509   the retrievals to the relative Akernel-smoothed radiosonde profiles can be used to minimize the

510   vertical representativeness effects due to the different vertical resolutions of these profiles, we

511   note that a statistical comparison between the four configurations of the observational vector

512   would not be fair if each of their retrieved profiles is compared to a different Akernel-smoothed

513   radiosonde profile. Therefore, in the statistical analysis presented later in the manuscript

514   (section 4.2), mean bias, root mean square error (RMSE), and Pearson correlation coefficients

515   will be computed between the various TROPoe retrieval configurations and the unsmoothed

516   radiosonde profiles, just interpolated to the same vertical levels of the retrieved profiles.

517   The **ATkernel** can help understand the differences in the retrieved temperature profiles

518   obtained by the configurations using additional RASS data, shown in the example of Fig. 2.

519   Figure 3a includes the temperature profiles of the radiosonde (unsmoothed and **ATkernel**'s

520   smoothed) and PRs of MWRzo and MWRzo449 for the same example as in Fig. 2. Due to the

521   inclusion of RASS measurements, the **ATkernel**-smoothed radiosonde profile of the MWRzo449

522   configuration (dashed light-blue line) is closer to the original radiosonde data (in red) compared

523   to the black dashed profile of the MWRzo's **ATkernel**-smoothed radiosonde profile.

524   Additionally, the rows of the **ATkernel** provide a measure of the retrieval smoothing as a

525   function of altitude, so the full-width half maximum (FWHM) of each **ATkernel** row estimates

526   the vertical resolution of the retrieved solution at each vertical level (Maddy and Barnet, 2008;

527   Merrelli and Turner, 2012). Plots of this vertical resolution as a function of the height for the

528   MWRzo PR and for the MWRzo449 PR are included in Fig. 3b. This plot shows that the

529   additional observations from the RASS 449 significantly improve the vertical resolution of the

530   retrievals.

531   The posterior covariance matrix, **Sop,** provides a measure of the uncertainty of the

532   retrievals while the square root of the diagonal of this matrix is used to specify the 1-σ errors in

533   the profiles of temperature or mixing ratio. Also, **Sop** shows the level-to-level dependency of

534   the retrievals, and in an ideal case should have all non-diagonal elements equal to zero.

535   Converted to a correlation matrix, it is possible to visualize these dependencies, as presented in

536   Fig. 3c, d. The use of additional RASS data (MWRzo449 **Sop**, Fig. 3d) reduces the off-diagonal

537   covariances, therefore substantially decreasing the correlations in those areas compared to the

538   MWRzo **Sop** (Fig. 3c).
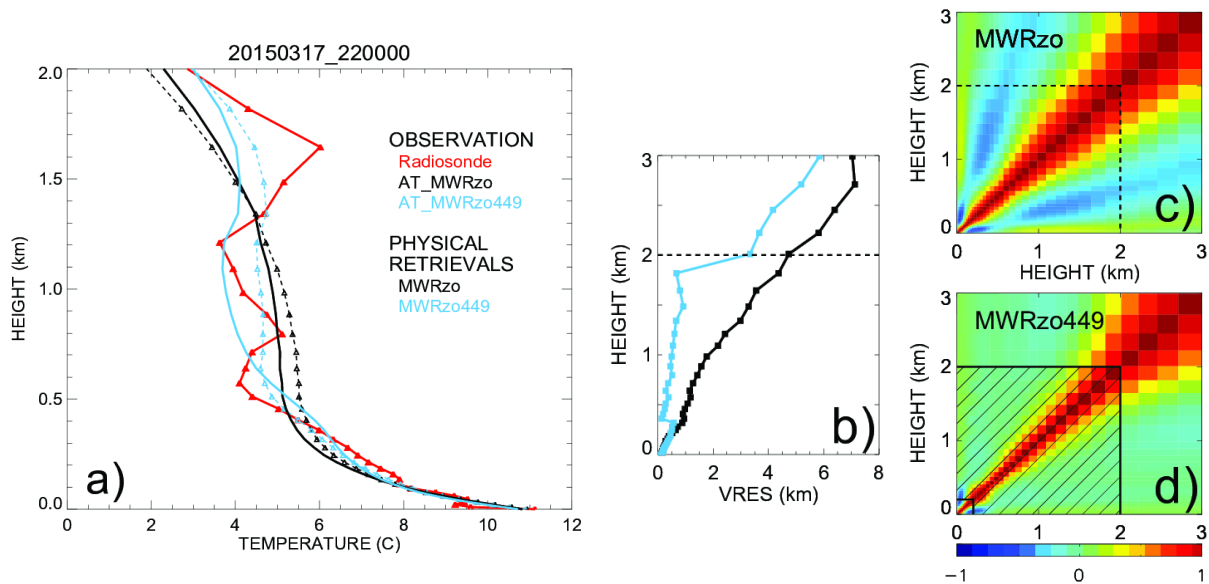
539

*540   Fig. 3. a) observed temperature profiles from radiosonde, in red, from **ATkernel**s smoothed*

*541   radiosonde, **AT_MWRzo** in dashed black, and **AT_MWRzo449** in dashed light-blue; PRs from*

542   MWRzo PR in solid black, and from MWRzo449 PR in solid light-blue. b) vertical resolution

543   (VRES) as a function of the height for the MWRzo PR (black), and for the MWRzo449 PR (light-

*544   blue). c) and d) 3 x 3 km (37 x 37 levels) **Sop** matrices, converted to correlation matrices, for the*

545   MWRzo PR (c), and for the MWRzo449 PR (d). Dashed lines on plots b)-d) mark 2 km AGL.

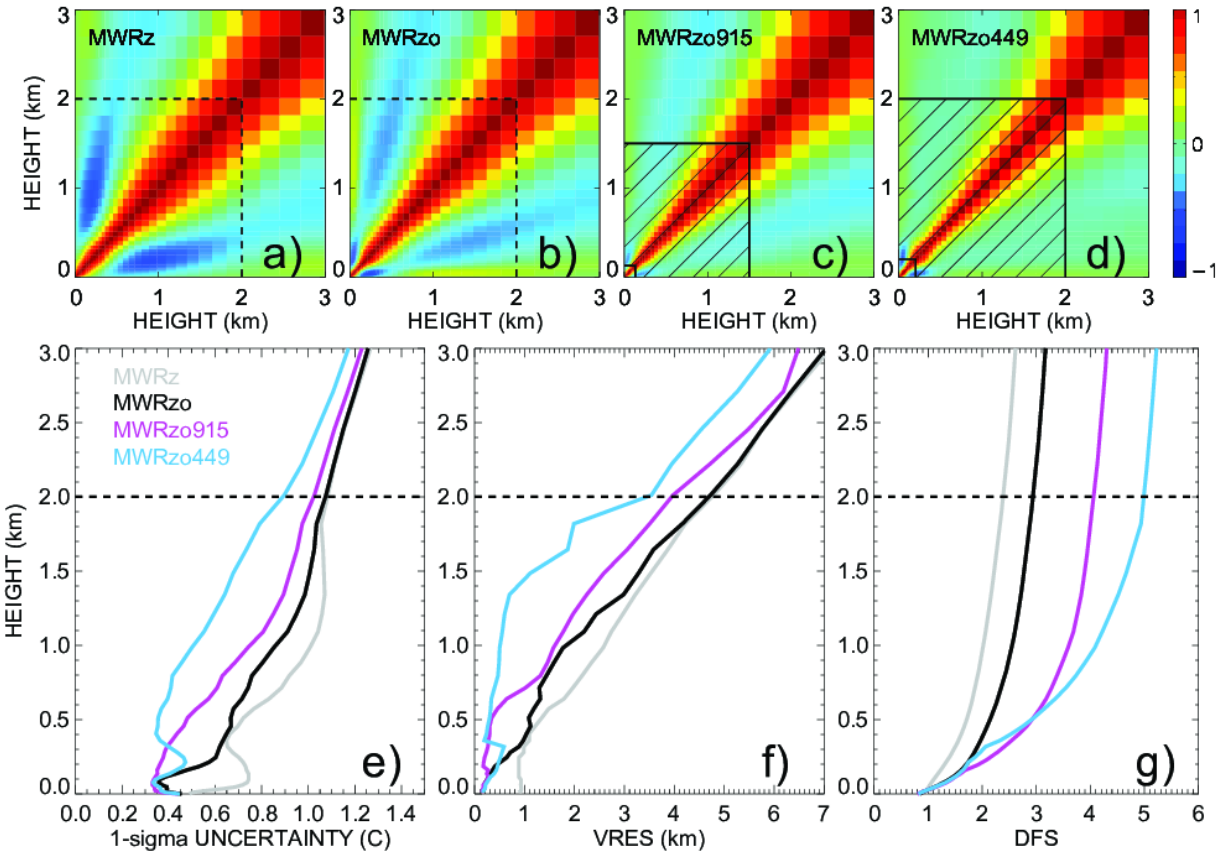*546   Hatched area on panel d marks the RASS measurement heights.*

547

548   To understand the level-to-level correlations among the 4 different retrieval

549   configurations in Table 1, the **Sop** matrices were averaged over all radiosonde events, and

550   converted to correlation matrices (Fig. 4). A clearly visible narrowing of the spread around the

551   main diagonal and correlation reduction in the off-diagonal elements result by adding

552   additional observations, from MWR zenith only (Fig. 4a), to MWR zenith-oblique (Fig. 4b), to

553   the larger impact obtained by the usage of the RASS 915 (Fig. 4c), concluding with the RASS 449

554   (Fig. 4d) data. The mean retrieval uncertainty profile for each of the PR configurations is

555   presented in Fig. 4e. The uncertainty of the MWRzo449 retrieval up to 1 km AGL is around 0.5

556   ^{o}C while the other retrievals have higher uncertainties of up to 1 ^{o}C. The higher accuracy of the

557   MWRzo449 retrievals is because that configuration has more observational information

558   compared to the other retrieval configurations.

559   Other statistically important features to analyze in the PRs, besides their uncertainty,

560   are the vertical resolution already introduced in the example of Fig. 3b, and the degree of

561   freedom for signal (DFS). These two features, derived from the **Akernel**s of each PR

562   configuration, averaged over all radiosonde events, are shown in Fig 4f and 4g. The vertical

563   resolution (Fig. 4f) shows the width of the atmosphere layer used for each retrieval height,

564   computed as the full-width half-maximum value of the averaging kernel. The cumulative DFS

565   profile (Fig. 4g) is a measure of the number of independent pieces of information in the

566   observations below the specified height. For example, at the 1 km AGL level the vertical

567   resolution of MWRzo449 is 0.5 km (i.e. information is from +/- 0.5 km around the retrieval

568   height is considered in the retrieval), while all other retrievals use the information from more

569   than +/- 1.5 km. Also, the DFS, as a cumulative measure, shows an increase in pieces of

570   information from MWRz to MWRzo for the whole profile and from MWRzo to MWRzo915 and

571   to MWRzo449 above ~0.2 km where RASS data are available. The DFS of MWRzo915 is higher

572   compared to the DFS of MWRzo449 in the 0.2-0.5 km AGL layer because RASS 915 data have

573   denser measurements there. It is also important to note that there is no additional information

574   added to any of the retrievals above 2km AGL, i.e. the slope of the cumulative DFS profiles are

575   equal. Despite that, the statistical analysis of the PRs up to 3 km AGL, shown in Section 4, will

576   prove that the retrieval improvements obtained by including the RASS are found even above

577   the height of the RASS measurements availability.

578

580   Fig. 4. Top row: The mean **Sop**s, displayed as correlation matrices, for (a) MWRz, (b) MWRzo, (c)

581   MWRzo915, and (d) MWRzo449, averaged over all radiosonde events. Hatched area on panels

582   c) and d) marks the RASS maximum measurement heights. Bottom panels: (e) one-sigma

583   uncertainty derived from the posterior covariance matrix in ^{o}C, (f) vertical resolution (VRES) in

584   km, and (g) cumulative Degree of Freedom (DFS) as a function of height for temperature,

585   averaged over all radiosonde events (MWRz is in gray, MWRzo is in black, MWRzo915 is in

586   purple, and MWRzo449 is in light-blue). Dashed lines mark 2 km AGL on all panels.

587

588   The improvements from MWRz (in gray) to MWRzo (in black), to MWRzo915 (in purple),

589   and finally to MWRzo449 (in light-blue) are visible in all three panels (Fig 4e-g), whereas

590   MWRzo449 has the lowest 1-σ uncertainty and highest DFS compared to the other PRs,

591   particularly below 2 km AGL, where RASS 449 measurements are available. Finally, it is

592   interesting that below 200 m AGL the MWRzo915 has slightly smaller lowest 1-σ uncertainty

593   and vertical resolution relative to the MWRzo449, as could be expected due to the first

594   available height of the RASS 915 being lower (120 m AGL) than the first available height for the

595   RASS 449 (217 m AGL) and due to the finer vertical resolution of the 915-MHz RASS. This

596   suggests that if additional observations were available in the lowest several 100 m of the

597   atmosphere where RASS measurements are not available, improvements might be even better

598   closer to the surface, where temperature inversions, if present, are sometimes difficult to

599   retrieve correctly.

600

601   **4. Results**

602   **4.1 Statistical analysis of physical retrievals up to 3km AGL**

603   Several cases were found during XPIA when the temperature profile exhibited

604   inversions, with the lowest happening in the surface layer. Figure 5 shows one of the most

605   complex cases, with several temperature inversions visible in the temperature profile from the

606   radiosonde (red line), in the temperature measurements from the BAO tower (blue squares),

607   and in the virtual temperature measured by the RASS 449 (light blue triangles). Note that the

608   virtual temperature profile is in close agreement with the temperature measured by
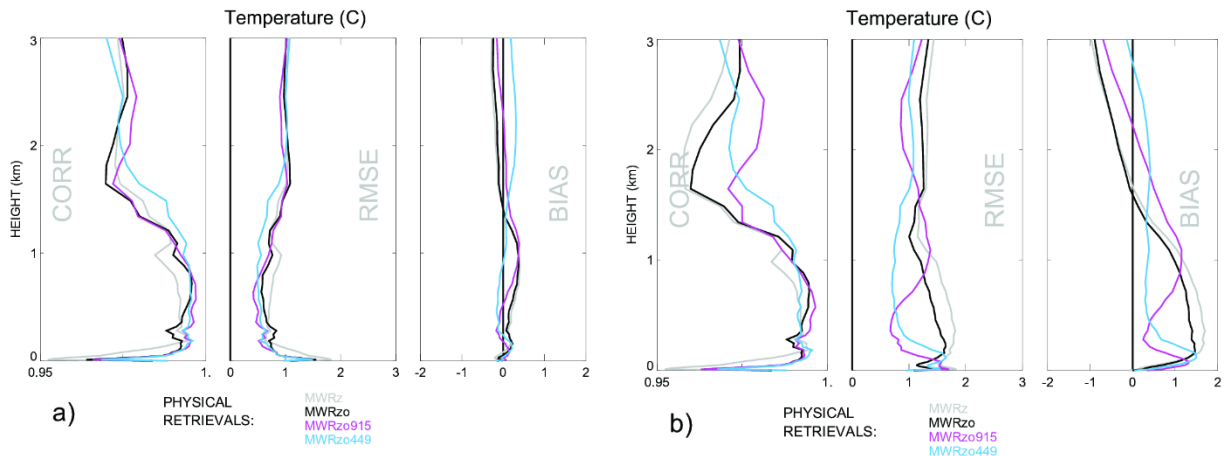
609   radiosonde.
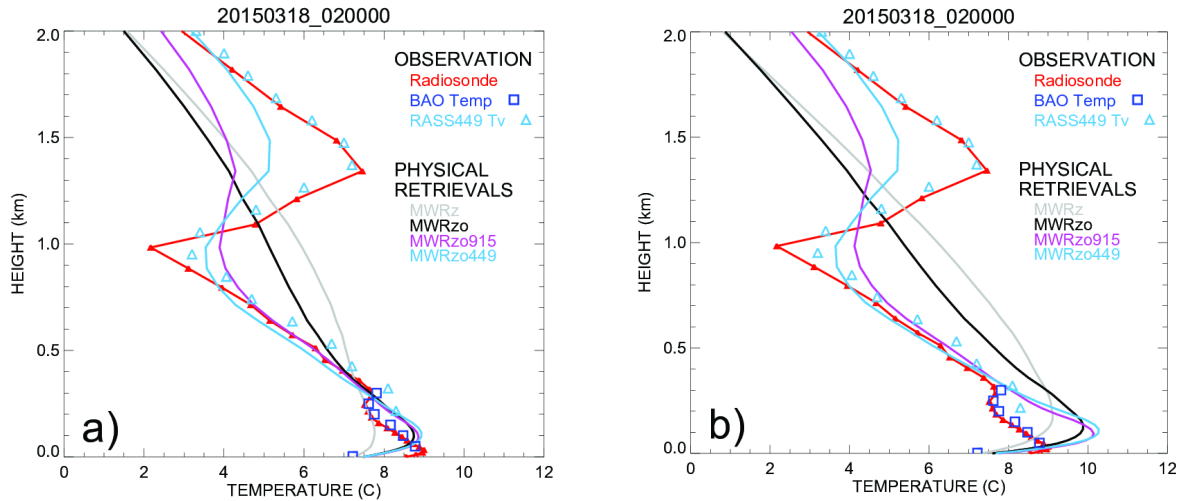
Fig. 5. As in Fig. 2 but for 18 March 2015 at 0200 UTC. The RASS 449 virtual temperature is

included as light blue triangles. a) shows the PRs obtained after applying the radiosonde BC, and

b) shows the PRs obtained after applying the TROPoe BC on the MWR Tbs.

Figure 5 also illustrates the difference in the temperature profiles, especially between 0-

300m AGL, for the two different bias-correction schemes, which show noticeable differences in

the biases of the opaque channels (especially important for the near-ground retrievals)

presented in Fig. 1. As expected, the radiosonde BC method yielded a retrieved profile closer to

the radiosonde temperature profile than when using TROPoe BC, for which the inversion in the

temperature profile close to the surface is too accentuated (particularly the black, purple, and

cyan lines, all of which used oblique scan data).

The relative statistical behavior (Pearson correlation, RMSE, and bias) of the PRs for

both temperature and mixing ratio against radiosondes is shown in Figure 6, using both bias-

correction approaches. PRs obtained after applying the radiosonde BC (Fig. 6a) present overall

625   smaller RMSE and bias (the latter almost equal to zero up to 3 km AGL) and slightly higher

626   correlations compared to the statistics of the PRs obtained after applying the TROPoe BC (Fig.

627   6b). This could be expected since for the comparison in Fig. 6a a subset of the radiosondes were

628   already used for the Tb bias correction. Also, the different retrievals show a narrower

629   distribution for the panels in Fig. 6a. Nevertheless, the results obtained when applying either

630   bias-correction methods (in Fig. 6a, b) consistently show the improvement obtained when the

631   RASS observations are used, with relatively smaller bias and RMSE in the 3 km layer AGL. The

632   correlation is mainly improved above 1 km, when RASS observations are included.

633   *Fig. 6. Pearson correlation, RMSE, and mean bias for temperature profiles of MWRz in gray,*

634   *MWRzo in black, MWRzo915 in purple, and MWRzo449 in light-blue for the radiosonde BC bias-*

635   *correction method in a) and TROPoe BC method in b).*

636

637   Besides temperature profiles, the PRs also provide water vapor mixing ratio profiles. It is

638   understandable that the different configurations of PRs are not noticeably different from each

639   other in relation to moisture, because the Tv observations from the RASS are dominated by the

640   ambient temperature (not moisture), and thus have little impact on the water vapor retrievals.

641   We found that the **AQKernel**s are almost identical for all four PR configurations (not shown).

642   Detailed statistical evaluation of the PRs mixing ratio profiles are presented in Fig, 7, also

643   averaged over all radiosonde events, and show very similar correlations, RMSEs, and biases for

644   all PRs, implying that the impact of including RASS observations in the retrieval is minimal on

645   this variable. Finally, it is noted that Fig. 7 shows the mixing ratio of the data from TROPoe BC.

646   The radiosonde BC mixing ratio results are almost identical.
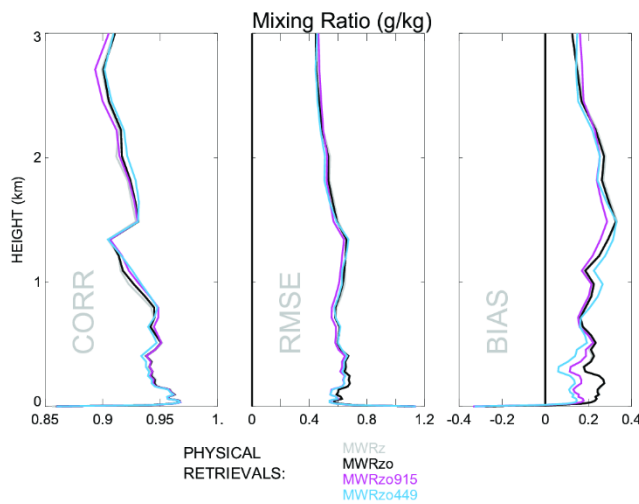
648
649
650
651
652
653

654   *Fig. 7. Same as the panels in Fig. 6b, but for mixing ratio, when using the TROPoe BC method on*

655   *the MWR Tbs.*

656

657   **4.2 Statistics for the profiles least close to the climatology**

658   Physical retrievals use climatological data as a constraint in the retrieval. Statistically,

659   the averaged profiles of both temperature and moisture variables are very close to the

660   climatological averages. However, the most interesting and difficult profiles to retrieve are the

661   cases furthest from climatology (Löhnert and Maier, 2012). To check the behavior of the

662   retrieved data in such "extreme" cases, the RMSE was first calculated for each radiosonde

663 profile relative to the prior profiles for 37 vertical levels from the surface up to 3 km AGL, and

664 then the 15 cases with the largest 0-3 km layer averaged RMSEs compared to the prior were

665 selected.
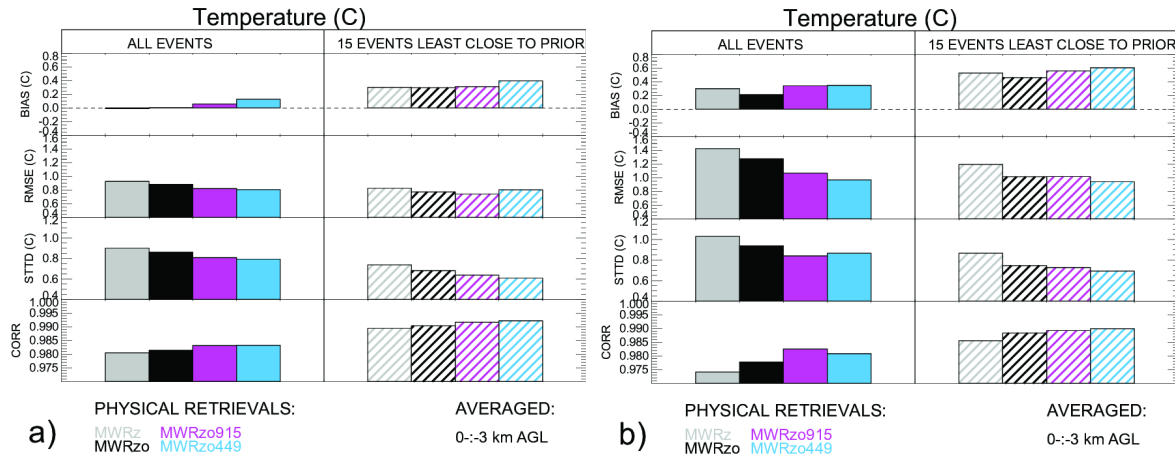
666 *Fig. 8. From top to bottom: biases (retrievals minus radiosonde), RMSEs, standard deviations of*

667 *the difference between retrievals and radiosonde, and Pearson correlations for the four PR*

668 *configurations, averaged from the surface to 3 km AGL, and over all radiosonde data (solid*

669 *boxes), and over the 15 extreme cases (hatched boxes). The data in panels a) use radiosonde BC,*

670 *and in b) TROPoe BC on the MWR Tbs.*

671 Figure 8 shows the temperature statistical analysis for the entire radiosonde data set

672 (solid boxes) and for the fifteen events far from the climatological mean (hatched boxes) for

673 bias, RMSE, standard deviation of the differences between retrievals and radiosonde data, and

674 Pearson correlation, calculated as the weighted averaged over the 37 vertical heights up to 3

675 km AGL[1].

---

[1] The vertical grid used in the PRs is not uniform, with more frequent levels closer to the surface. If a simple average of the data from all levels is used, the near-surface layer will be weighted more compared to the upper levels of the retrievals. To avoid this, a vertical average over the lowest 3 km AGL is performed using weights at each vertical level determined by the distance between the levels.

676   Differences in the statistics when using the entire radiosonde data set or the fifteen

677   extreme profiles are noticeable for all statistical estimators. The PRs that include RASS

678   observations show better performance compared to the strictly MWR-only PR profiles (i.e.,

679   MWRz and MWRzo) for almost all statistical comparisons. This improvement is larger for the

680   PRs using the TROPoe BC (Fig. 8b) compared to the PRs using the radiosonde BC (Fig. 8a). Three

681   statistical estimators, RMSE, standard deviation, and Pearson correlation show overall better

682   values for the 15 extreme cases compared to the whole radiosonde dataset, for all PR

683   configurations and both BC approaches. This is due to the fact that for this dataset the monthly

684   averaged radiosonde profiles (for March and May particularly) depart quite substantially from

685   the monthly prior profiles. For example, the averaged radiosonde profile in March is warmer by

686   ~7 ^{o}C compared to the March prior (and in May by ~5 ^{o}C) in the first 3 km AGL. Consequently,

687   the extreme cases (mostly found in March) have the warmest radiosonde temperature profiles,

688   but are overall closer to the monthly averaged radiosonde profiles.

689   Table 2 includes the same data as in Figure 8 but as a percentage of the improvement,

690   compared to the MWRz retrievals.

691

692

693

694

695

696

0-3 km AGL	ALL EVENTS					15 EVENTS LEAST CLOSE TO THE PRIOR			
	RADIOSONDE BIAS-CORRECTION								
	MWRz	MWRzo	MWRzo RASS915	MWRzo RASS449		MWRz	MWRzo	MWRzo RASS915	MWRzo RASS449
RMSE	0%	5%	11%	13%		0%	7%	10%	3%
STTD	0%	4%	10%	12%		0%	8%	14%	17%
CORR	0%	0.1%	0.3%	0.3%		0%	0.1%	0.2%	0.3%
	TROPoe BIAS-CORRECTION								
RMSE	0%	10%	25%	32%		0%	15%	15%	21%
STTD	0%	9%	18%	16%		0%	14%	16%	20%
CORR	0%	0.4%	0.9%	0.7%		0%	0.3%	0.4%	0.4%

697

698   *Table 2. Retrieval improvements for different RASS/MWR configurations as a percentage*

699   *compared to MWRz.*

700

701   The results presented in Table 2 show improvements in all statistical estimations when

702   including RASS observations, with improvements in RMSE between 10 and 20 %, demonstrating

703   the positive impact derived by the inclusion of the active measurements, regardless of the bias-

704   correction method used, but larger for the TROPoe BC data because there is more room for

705   improvement when this BC method is used. Improvements in the Pearson correlation

706   coefficients are small because correlation, determined during XPIA by the overall temperature

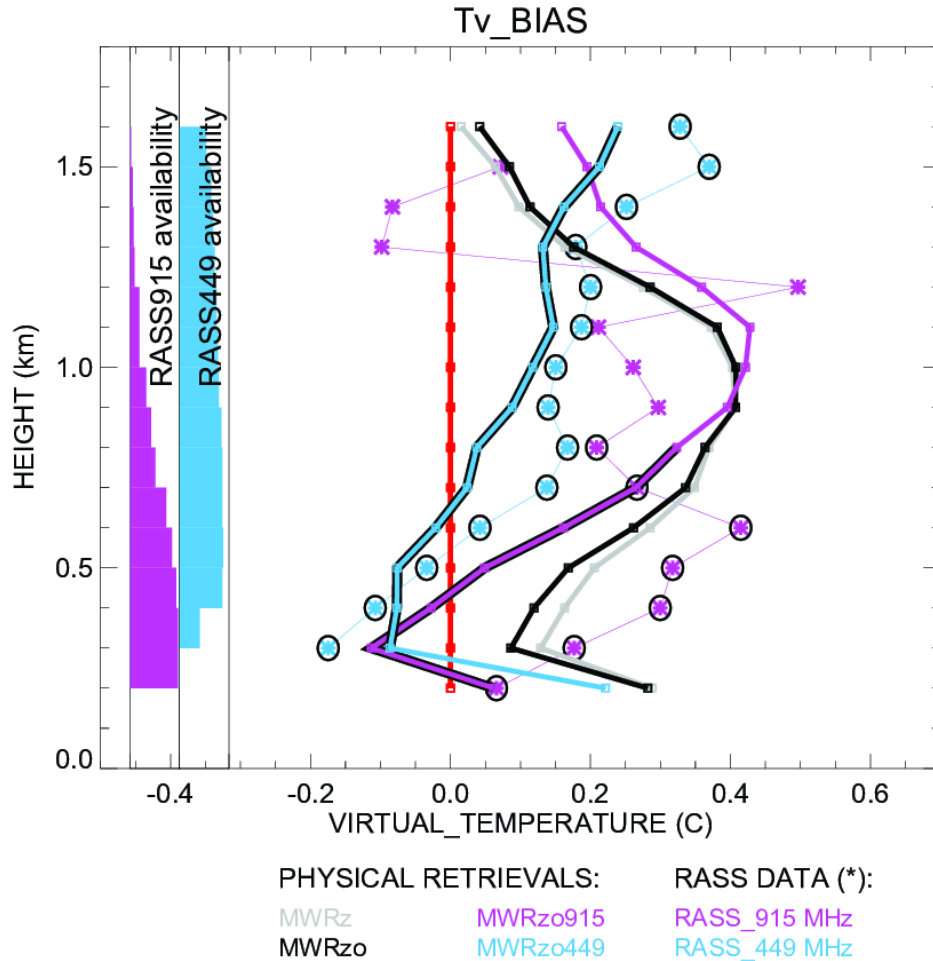707   structure with height and diurnal cycle, is already good, leaving little room for improvement.

708

709   **4.3 Virtual temperature profile statistics**

710   Using the physical retrieval outputs, "retrieved virtual temperature profiles" can also be

711   calculated. In this section the direct comparison of these retrieved virtual temperature profiles

712   and RASS virtual temperature profiles to the original radiosonde is shown. With this comparison

713   we want to show how the biases of the retrieved profiles relate to the original RASS Tv biases.

714   Figure 9 shows Tv retrieved profile biases compared to the original radiosonde data as

715   solid lines, and RASS 915 and RASS 449 Tv bias as asterisks. RASS data are interpolated on a

716   regular vertical grid, going from 200 m to 1.6 km with a 100 m range, for easy comparison.

717   A zero bias is denoted by the red line. On the left side of the figure the bar charts of the

718   RASS measurement availability are shown as a function of height. The widest part of these

719   charts corresponds to 100% data availability. Heights with RASS availability greater than 50%

720   are marked with additional circles over the asterisks.

Tv_BIAS

PHYSICAL RETRIEVALS: RASS DATA (*):
MWRz   MWRzo915   RASS_915 MHz
MWRzo   MWRzo449   RASS_449 MHz

721

722   *Fig. 9. Bias of virtual temperature for all PR configurations compared to the original radiosonde*

723   *measurements. RASS data are marked by asterisks and by additional circles for the RASS data*

724   *with more than 50% availability, according to the availability bar charts on the left.*

725   *All PRs profiles are derived after applying the radiosonde BC method.*

726

727   While RASS 449 data are available at almost all heights up to 1.6 km, the RASS 915 data

728   availability decreases considerably with height, lowering to 50% availability around 800 m AGL.

729   The PRs that include RASS data, MWRzo915 and MWRzo449, are also marked with additional

730 black lines at the heights with at least 50% of relative RASS data availability. In agreement with

731 Fig. 6a, this figure clearly shows the superiority of the MWRzo449 and MWRzo915 (in the layer

732 with > 50% RASS data availability) compared to the MWRz and MWRzo configurations, which

733 do not include RASS data. For MWRzo449, RASS 449 data were almost always available,

734 therefore it is easy to identify a similarity between the Tv bias profiles of the RASS 449 and the

735 PRs including it. Thus, for the MWRzo449 the Tv bias is more uniform through the heights

736 compared to all other PRs that do not include RASS data. Moreover, it is noted a roughly

737 constant offset between the MWRzo449 Tv and RASS 449 Tv biases profiles, with their

738 averaged difference equal to ~0.08 $^\circ$C (when the radiosonde BC is used), and to ~0.32 $^\circ$C (when

739 the TROPoe BC is used, not shown), over the ~1.3 km (0.3-1.6 km) atmospheric layer where

740 more than 50% of the RASS 449 measurements are available, uniformly distributed through the

741 heights. The inclusion of the RASS into the PRs does reduce the values of the biases in the

742 retrievals even below the values of the RASS biases.

743

744 **5. Conclusions**

745   In this study, data collected during the XPIA field campaign were used to test different

746 configurations of a physical-iterative retrieval (PR) approach in the determination of

747 temperature and humidity profiles from data collected by microwave radiometers, surface

748 sensors, and RASS measurements. The accuracy of several PR configurations was tested: two

749 configurations made use only of surface observations and MWR observed brightness

750 temperature (zenith only, MWRz; and zenith plus oblique, MWRzo); while two others included

751 the active virtual temperature profile observations available from co-located RASS (one, RASS

752 915, associated with a 915-MHz; and the other, RASS 449, associated with a 449-MHz wind

753 profiling radar). Radiosonde launches were used for verification of the retrieved profiles. In

754 Appendix A, the performance of MWRz and MWRzo retrieved profiles and Neural Network

755 retrieved profiles against the radiosondes was evaluated.

756   To remove any observational systematic error in the MWR Tb observations, two bias-

757 correction procedures were tested. The first one takes advantage of the many radiosondes

758 launched during XPIA, and the second one uses climatological profiles. As expected, the

759 radiosonde bias-correction method gives retrieved profiles closer to the radiosonde

760 temperature profiles than when using the climatological based method. Nevertheless, our

761 results show that regardless of the bias-correction method used, the inclusion of the

762 observations from the active RASS instruments in the PR approach improves the accuracy of the

763 temperature profiles by around 10-20% compared to the PR configuration using only surface

764 observations and MWR observed brightness temperature from the zenith scan. Of the PRs

765 configurations tested, generally better statistical agreement is found with the radiosonde

766 observations when the RASS 449 is used together with the surface observations and brightness

767 temperature from the zenith and averaged oblique MWR observations.

768   The **AKernel** and the posterior covariance matrices for temperature are used to derive

769 the one-sigma uncertainty, vertical resolution, and cumulative degree of freedom as a function

770 of height for the different PRs, and the level-to-level correlated uncertainty of the retrievals.

771 Results show that the inclusion of the active instruments improves all of the above-mentioned

772 variables in the 0-3km layer, including at heights between 2-3km that are above the maximum

773   RASS height. Thus, the positive impact of the RASS observations extends into the atmosphere

774   above the height of measurements themselves.

775   Furthermore, 15 cases when temperature profiles from the radiosonde observations

776   were the furthest away from the mean climatological average were selected, and the statistical

777   comparison was reproduced over this subset of cases. These are the cases usually the most

778   difficult to retrieve and the most important to forecast; therefore, it is essential to improve the

779   retrievals in these situations. Even for this subset of selected cases the inclusion of active

780   sensor observations in the PRs is found to be beneficial.

781   Finally, the impact of the inclusion of RASS measurements on the retrieved humidity

782   profiles was considered, but the inclusion of RASS observations did not produce significantly

783   better results, compared to the configurations that do not include them. This was not a surprise

784   as RASS measures virtual temperature, effectively adding very little extra information to the

785   water vapor retrieval. In this case a better option would be to consider adding other active

786   remote sensors such as water vapor differential absorption lidars (DIALs) to the PRs. Turner and

787   Löhnert (2021) showed that including the partial profile of water vapor observed by the DIAL

788   substantially increases the information content in the combined water vapor retrievals.

789   Consequently, to improve both temperature and humidity retrievals a synergy between MWR,

790   RASS, and DIAL systems would likely be necessary.

791

792   **Appendix A**

793   The neural network (NN) retrievals developed by the vendor explicitly for XPIA use a

794   training dataset based on a 5-year climatology of profiles from radiosondes launched at the

795 Denver International Airport, 35 miles south-east from the XPIA site. NN-based MWR vertical

796 retrieval profiles were obtained using the zenith or an average of two oblique elevation scans,

797 15- and 165-degrees (not including the zenith), all with 58 levels extending from the surface up

798 to 10 km, with nominal vertical grid depending on the height (every 50 m from the surface to

799 500 m, every 100 m from 500 m to 2 km, and every 250 m from 2 to 10 km, AGL).

800 Fig. 1A shows composite NN vertical profiles of temperature (separately for the zenith

801 and averaged obliques) calculated for radiosonde launch times, and the corresponding PR

802 profiles already introduced in Fig. 6a, b. For a proper comparison, only MWRz and MWRzo

803 profiles are used, without including RASS measurements. It has to be noted that since the "NN

804 oblique" retrieval provided by the manufacturer of the radiometer does not include the zenith,

805 this configuration cannot be considered exactly equivalent to the MWRzo PR.

808

809

810

811

812

813

814

815

43
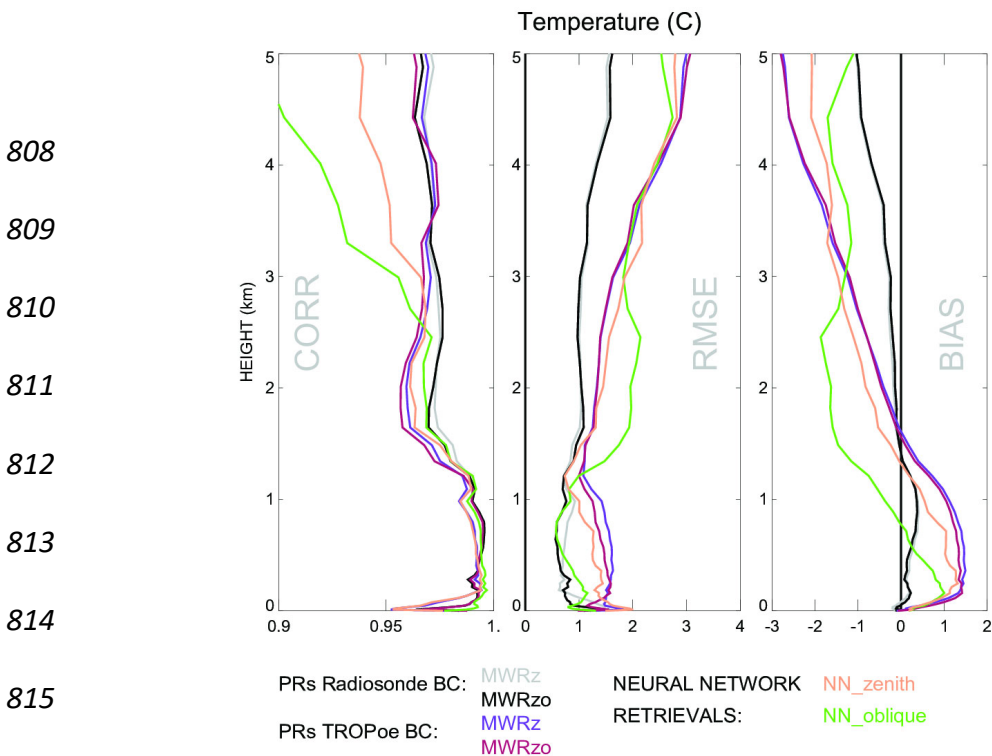
816   *Fig. 1A. Pearson correlation, RMSE, and mean bias for temperature profiles for MWRz in grey*

817   *(and purple) and MWRzo in black (and maroon) when the radiosonde BC (and the TROPoe BC)*

818   *method is applied. Included in this figure are the NN temperature profiles, from the zenith scan*

819   *(in beige), and from the averaged oblique scans (in green).*

820

821   Another difference to point out is that, while the MWR Tb data have been bias-

822   corrected before being used in the PR configurations, as discussed in Section 3.2, the NN

823   retrievals use the uncorrected Tb, since it was non-trivial to reprocess those retrievals. Martinet

824   et al. (2015) showed that when it is possible to bias-correct the MWR Tb before applying the

825   NN retrieval technique, the NN retrievals are not impacted below 1 km AGL, but a clear

826   improvement of NN retrievals in terms of RMSE and bias are observed between 1 and 3 km

827   altitude. As is visible in Fig. 1A, this is the layer of the atmosphere where the NN profiles (beige

828   and green lines) have larger bias and RMSE, compared to the PR profiles.

829   When the radiosonde BC method is used, the MWRz and MWRzo PRs (gray and black

830   lines) present better statistics through the entire profiles shown in Fig. 1A, with larger values of

831   the correlation coefficient, and smaller values of RMSE and bias. The oblique only NN profiles

832   (in green) show comparable statistics to the PRs employing the radiosonde BC method up to 1

833   km AGL, with degraded performances above this height. Above 1 km AGL, the zenith NN

834   profiles (in beige) do better than the oblique NN in terms of RMSE and bias. When the TROPoe

835   BC method is used, the MWRz and MWRzo PRs (purple and maroon lines) perform better than

836   the NN profiles only in terms of RMSE and bias, and above around 1.5 km AGL.

837   The better performance obtained by the MWRz and MWRzo PRs that use the

838   radiosonde BC approach demonstrate the importance of having an accurate and reliable

839   method for bias correcting the MWR.

840

841   **Data availability**

842   All data are publicly accessible at the DOE Atmosphere to Electrons Data Archive and

843   Portal, found at https://a2e.energy.gov/projects/xpia (Lundquist et al., 2016).

844

845   **Author contribution**

846   Irina Djalalova completed the primary analysis using the XPIA dataset. Daniel Gottas

847   contributed to the post-processing of the RASS data. Dave Turner modified the TROPoe

848   algorithm to include the RASS data as input. All authors contributed to the analysis of the

849   results. Irina Djalalova prepared the manuscript with contributions from all co-authors.

850

851   **Acknowledgements**

858

859   **Competing interests** The authors declare no competing interests.

860

861   **References**

862   Adachi, A. and H. Hashiguchi: Application of parametric speakers to radio acoustic sounding

863   system. **ATMOS MEAS TECH**, **12**, 5699–5715, https://doi.org/10.5194/amt-12-5699-

864   2019, 2019.

865   Adler, B., J. M. Wilczak, L. Bianco, I. Djalalova, J. B. Duncan Jr., D. D. Turner: Observational case

866   study of a persistent cold air pool and gap flow in the Columbia River Basin. **J APPL**

867   **METEOROL CLIM**, 60, 1071-1090, https://doi.org/10.1175/JAMC-D-21-0013.1, 2021.

868   Banta, R. M., and coauthors: Characterizing NWP model errors using Doppler lidar

869   measurements of recurrent regional diurnal flows: Marine-air intrusions into the

870   Columbia River Basin. **MON WEATHER REV**, **148**, 927-953,

871   https://doi.org/10.1175/MWR-D-19-0188.1, 2020.

872   Bianco L., D. Cimini, F. S. Marzano, and R. Ware: Combining microwave radiometer and wind

873   profiler radar measurements for high-resolution atmospheric humidity profiling, **J**

874   **ATMOS OCEAN TECH**, **22**, 949–965, https://doi.org/10.1175/JTECH1771.1, 2005.

875   Bianco, L., K. Friedrich, J. M. Wilczak, D. Hazen, D. Wolfe, R. Delgado, S. Oncley, and J. K.

876   Lundquist: Assessing the accuracy of microwave radiometers and radio acoustic

877   sounding systems for wind energy applications. **ATMOS MEAS TECH**, **10**, 1707-1721,

878   https://doi.org/10.5194/amt-10-1707-2017, 2017.

879   Cadeddu, M. P., J. C. Liljegren, and D. D. Turner: The Atmospheric radiation measurement

880   (ARM) program network of microwave radiometers: instrumentation, data, and

881   retrievals, **ATMOS MEAS TECH**, **6**, 2359–2372, https://doi.org/10.5194/amt-6-2359-

882   2013, 2013.

883   Cimini, D., T. J. Hewison, L. Martin, J. Guldner, C. Gaffard, F. S. Marzano: Temperature and

884   humidity profile retrievals from ground-based microwave radiometers during TUC,

885   **METEOROL Z**, Vol. 15, No. 5, 45-56, DOI: 10.1127/09411-D-2948/2006/0099, 2006.

886   Cimini, D., E. Campos, R. Ware, S. Albers, G. Giuliani, J. Oreamuno, P. Joe, S. E. Koch, S. Cober,

887   and E. Westwater: Thermodynamic Atmospheric Profiling during the 2010 Winter

888   Olympics Using Ground-based Microwave Radiometry, **IEEE T GEOSCI REMOTE**, **49**, 12,

889   https://doi.org/10.1109/TGRS.2011.2154337, 2011.

890   Cimini, D., Rosenkranz, P. W., Tretyakov, M. Y., Koshelev, M. A., and Romano, F.: Uncertainty of

891   atmospheric microwave absorption model: impact on ground-based radiometer

892   simulations and retrievals, **ATMOS CHEM PHYS**, **18**, 15231–15259,

893   https://acp.copernicus.org/articles/18/15231/2018, 2018.

894   Cimini, D., M. Haeffelin, S. Kotthaus, U. Löhnert, P. Martinet, E. O'Connor, C. Walden, M.

895   Collaud Coen, and J. Preissler: Towards the profiling of the atmospheric boundary layer

896   at European scale—introducing the COST Action PROBE. **Bulletin of Atmospheric**

897   **Science and Technology**, **1**, 23–42, https://doi.org/10.1007/s42865-020-00003-8, 2020.

898   Clough, S.A., M. W. Shephard, E. J. Mlawer, J. S. Delamere, M. Iacono, K. E. Cady-Pereira, S.

899   Boukabara and P. D. Brown: Atmospheric radiative transfer modeling: A summary of the

900   AER codes, **J QUANT SPECTROSC RA**, vol 91, no. 2, pp 233-244,

901   https://doi.org/10.1016/j.jqsrt.2004.05.058, 2005.

902   Crewell, S., U. Löhnert: Accuracy of Boundary Layer Temperature Profiles Retrieved With

903   Multifrequency Multiangle Microwave Radiometry, **IEEE T GEOSCI REMOTE**, VOL. 45,

904   NO. 7, JULY 2007, DOI: 10.1109/TGRS.2006.888434, 2007.

905   Engelbart, D., W. Monna, J. Nash: Integrated Ground-Based Remote-Sensing Stations for

906   Atmospheric Profiling, **COST Action 720 Final Report**, EUR 24172,

907   https://doi.org/10.2831/10752, 2009.

908   Görsdorf, U., and V. Lehmann: Enhanced Accuracy of RASS-Measured Temperatures Due to an

909   Improved Range Correction. **J ATMOS OCEAN TECH**, **17 (4)**, 406–416,

910   https://doi.org/10.1175/1520-0426(2000)017<0406:EAORMT>2.0.CO;2, 2000.

911   Han, Y., and E. R. Westwater: Remote sensing of tropospheric water vapor and cloud liquid

912   water by integrated ground-based sensors. **J ATMOS OCEAN TECH**, **12**, 1050-1059, DOI:

913   https://doi.org/10.1175/1520-0426(1995)012<1050:RSOTWV>2.0.CO;2, 1995.

914   Hewison, T.: 1D-VAR Retrieval of Temperature and Humidity Profiles From a Ground-Based

915   Microwave Radiometer, **IEEE T GEOSCI REMOTE**, **45(7)**, 2163–2168,

916   https://doi.org/10.1109/TGRS.2007.898091, 2007.

917   Horst, T. W., S. R. Semmer, and I. Bogoev: Evaluation of Mechanically-Aspirated

918   Temperature/Relative Humidity Radiation Shields, 18th Symposium on Meteorological

919   Observation and Instrumentation, AMS Annual Meeting, New Orleans, LA, 10-15

920   January 2016, https://ams.confex.com/ams/96Annual/webprogram/Paper286839.html,

921   2016.

922   Kaimal, J. C., and J. E. Gaynor: The Boulder Atmospheric Observatory. **J CLIM APPL METEOROL**,

923   **22**, 863–880, https://doi.org/10.1175/1520-0450(1983)022<0863:TBAO>2.0.CO;2, 1983.

924 Küchler, N., D. D. Turner, U. Löhnert,and S. Crewell: Calibrating ground-based microwave

925   radiometers: Uncertainty and drifts, **RADIO SCI**, **51**, 311–327,

926   doi:10.1002/2015RS005826, 2016.

927 Löhnert U. and O. Maier: Operational profiling of temperature using ground-based microwave

928   radiometry at Payerne: prospects and challenges. **ATMOS MEAS TECH**, **5**, 1121–1134,

929   https://doi.org/10.5194/amt-5-1121-2012, 2012.

930 Lundquist, J. K., J. M. Wilczak, R. Ashton, L. Bianco, W. A. Brewer, A. Choukulkar, A. Clifton, M.

931   Debnath, R. Delgado, K. Friedrich, S. Gunter, A. Hamidi, G. V. Iungo, A. Kaushik, B.

932   Kosović, P. Langan, A. Lass, E. Lavin, J. C.-Y. Lee, K. L. McCaffrey, R. K. Newsom, D. C.

933   Noone, S. P. Oncley, P. T. Quelet, S. P. Sandberg, J. L. Schroeder, W. J. Shaw, L. Sparling,

934   C. St. Martin, A. St. Pe, E. Strobach, K. Tay, B. J. Vanderwende, A. Weickmann, D. Wolfe,

935   and R. Worsnop: Assessing state-of-the-art capabilities for probing the atmospheric

936   boundary layer: the XPIA field campaign. **B AM METEOROL SOC**, **98**, 289–314,

937   https://doi.org/10.1175/BAMS-D-15-00151.1, 2017.

938 Maahn, M., D. D. Turner, U. Löhnert, D. J. Posselt, K. Ebell, G. G. Mace, and J. M. Comstock:

939   Optimal estimation retrievals and their uncertainties: What every atmospheric scientist

940   should know. **B AM METEOROL SOC**, **101**, E1512-E1523, https://doi.org/10.1175/BAMS-

941   D-19-0027.1, 2020.

942 Maddy, E. S. and C. D. Barnet: Vertical Resolution Estimates in Version 5 of AIRS Operational

943   Retrievals. **IEEE T GEOSCI REMOTE**, VOL. **46**, NO. 8, AUGUST 2008,

944   https://doi.org/10.1109/TGRS.2008.917498, 2008.

945   Martinet, P., A. Dabas, J.-M. Donier, T. Douffet, O. Garrouste, and R. Guillot: 1D-Var

946   temperature retrievals from microwave radiometer and convective scale model, **TELLUS**

947   **A**, **67:1**, https://doi.org/10.3402/tellusa.v67.27925, 2015.

948   Martinet, P., D. Cimini, F. Burnet, B. Ménétrier, Y. Michel, and V. Unger: Improvement of

949   numerical weather prediction model analysis during fog conditions through the

950   assimilation of ground-based microwave radiometer observations: a 1D-Var study,

951   **ATMOS MEAS TECH**, **13**, 6593–6611, https://doi.org/10.5194/amt-13-6593-2020, 2020.

952   May, P. T. and J. M. Wilczak: Diurnal and Seasonal Variations of Boundary-Layer Structure

953   Observed with a Radar Wind Profiler and RASS. **MON WEATHER REV**, **121**, 673–682,

954   https://doi.org/10.1175/1520-0493(1993)121<0673:DASVOB>2.0.CO;2, 1993.

955   Masiello, G., C. Serio, and P. Antonelli: Inversion for atmospheric thermodynamical parameters

956   of IASI data in the principal components space. **Q J ROY METEOR SOC**, **138**, 103–117,

957   https://doi.org/10.1002/qj.909, 2012.

958   Merrelli, A. M., and D. D. Turner: Comparing information content of upwelling far infrared and

959   midinfrared radiance spectra for clear atmosphere profiling. **J ATMOS OCEAN TECH**, **29**,

960   510–526, https://doi.org/10.1175/JTECH-D-11-00113.1, 2012.

961   Neiman, P. J., D. J. Gottas, and A. B. White: A Two-Cool-Season Wind Profiler–Based Analysis of

962   Westward-Directed Gap Flow through the Columbia River Gorge. **MON WEATHER REV**,

963   **147**, 4653-4680, https://doi.org/10.1175/MWR-D-19-0026.1, 2019.

964   North, E. M., A. M.Peterson, and H. D. Parry: RASS, a remote sensing system for measuring low-

965   level temperature profiles. **B AM METEOROL SOC**, **54**, 912–919, 1973.

966 Payne, V. H., J. S. Delamere, K. E. Cady-Pereira, R. R. Gamache, J.-L. Moncet, E. J. Mlawer, and S.

967   A. Clough: Air-broadened half-widths of the 22- and 183-GHz water-vapor lines. **IEEE T**

968   **GEOSCI REMOTE**, **46**, 3601-3617, https://doi.org/10.1109/TGRS.2008.2002435, 2008.

969 Payne, V. H., E. J. Mlawer, K. E. Cady-Pereira, and J.-L. Moncet: Water vapor continuum

970   absorption in the microwave. **IEEE T GEOSCI REMOTE**, **49**, 2194-2208,

971   https://doi.org/10.1109/TGRS.2010.2091416, 2011.

972 Rodgers, C. D.: Inverse Methods for Atmospheric Sounding: Theory and Practice. Series on

973   Atmospheric, Oceanic and Planetary Physics, Vol. 2, World Scientific, 238 pp, 2000.

974 Rosenkranz, P. W.: Water vapour microwave continuum absorption: A comparison of

975   measurements and models. **RADIO SCI**, **33**, 919–928,

976   https://doi.org/10.1029/98RS01182, 1998.

977 Shaw, W., and Coauthors: The Second Wind Forecast Improvement Project (WFIP 2): General

978   Overview. **B AM METEOROL SOC**, **100(9)**, 1687–1699, https://doi.org/10.1175/BAMS-D-

979   18-0036.1, 2019.

980 Solheim, F., J. R. Godwin, J., and R. Ware: Passive ground-based remote sensing of atmospheric

981   temperature, water vapor, and cloud liquid profiles by a frequency synthesized

982   microwave radiometer. **METEOROL Z**, **7**, 370–376, 1998a.

983 Solheim F., J. R. Godwin, E. R. Westwater, Y. Han, S. J. Keihm, K. Marsh, R. Ware: Radiometric

984   profiling of temperature, water vapor and cloud liquid water using various inversion

985   methods. **RADIO SCI**, **33**, 393–404, https://doi.org/10.1029/97RS03656, 1998b.

986 Stankov, B. B., E. R. Westwater, and E. E. Gossard: Use of wind profiler estimates of significant

987   moisture gradients to improve humidity profile retrieval. **J ATMOS OCEAN TECH**, **13**,

988   1285-1290, DOI:

989   https://doi.org/10.1175/15200426(1996)013<1285:UOWPEO>2.0.CO;2, 1996.

990   Strauch, R. G. , D. A. Merritt, K. P. Moran, K. B. Earnshaw, and D. V. De Kamp: The Colorado

991   wind-profiling network. **J ATMOS OCEAN TECH**, **1**, 37–49, https://doi.org/10.1175/1520-

992   0426(1984)001<0037:tcwpn>2.0.co;2, 1983.

993   Turner, D. D., and U. Löhnert: Information content and uncertainties in thermodynamic profiles

994   and liquid cloud properties retrieved from the ground-based Atmospheric Emitted

995   Radiance Interferometer (AERI). **J APPL METEOROL CLIM**, **53**, 752–771,

996   https://doi.org/10.1175/JAMC-D-13-0126.1, 2014.

997   Turner, D. D., and W. G. Blumberg: Improvements to the AERIoe thermodynamic profile

998   retrieval algorithm. **IEEE J-STARS**, **12(5)**, 1339–1354,

999   https://doi.org/10.1109/JSTARS.2018.2874968, 2019.

1000   Turner, D. D., and U. Löhnert: Ground-based Temperature and Humidity Profiling: Combining

1001   Active and Passive Remote Sensors. **ATMOS MEAS TECH**, **14**, 3033–3048,

1002   https://doi.org/10.5194/amt-2020-352, 2021.

1003   Ware R., Solheim F., Carpenter R., and Coauthors: A multi-channel radiometric profiler of

1004   temperature, humidity and cloud liquid. **RADIO SCI**, **38**, No. 4, 8079,

1005   https://doi.org/10.1029/2002RS002856, 2003.

1006   Weber, B. L., D. B. Wuertz, D. C. Welsh, and R. Mcpeek: Quality controls for profiler

1007   measurements of winds and RASS temperatures. **J ATMOS OCEAN TECH**, **10**, 452–464,

1008   https://doi.org/10.1175/1520-0426(1993)010<0452:qcfpmo>2.0.co;2, 1993.

1009   Wilczak, J. M., and Coauthors: The Second Wind Forecast Improvement Project (WFIP2):

1010   Observational Field Campaign. **B AM METEOROL SOC**, **100(9)**, 1701–1723,

1011   https://doi.org/10.1175/BAMS-D-18-0035.1, 2019.

1012   Wolfe, D. E. and R. J. Lataitis: Boulder Atmospheric Observatory: 1977–2016: The end of an era

1013   and lessons learned. **B AM METEOROL SOC**, **99**, 1345–1358,

1014   https://doi.org/10.1175/BAMS-D-17-0054.1, 2018.